iScience

CellPress
OPEN ACCESS

Article

# Flat clathrin lattices are linked to metastatic potential in colorectal cancer

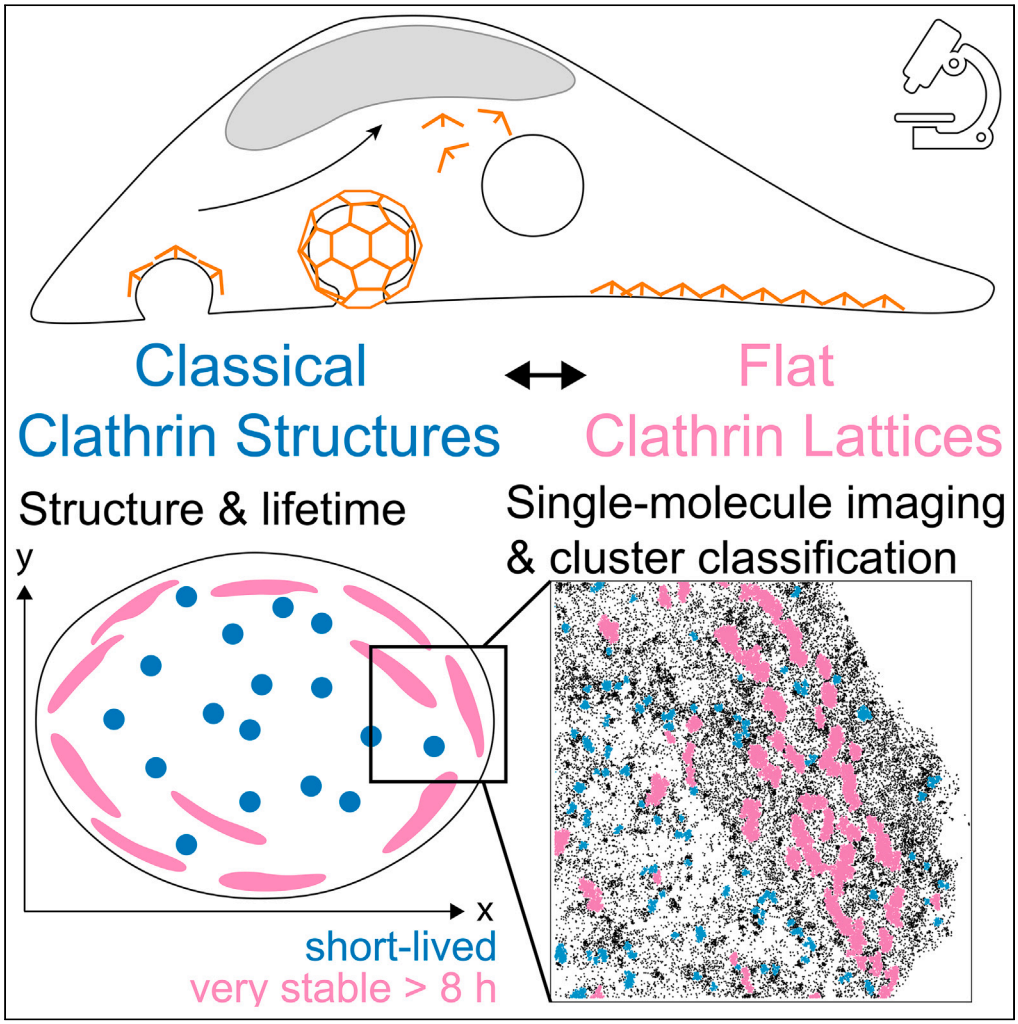


Charlotte Cresens, Guillermo Solís-Fernández, Astha Tiwari, Rik Nuyts, Johan Hofkens, Rodrigo Barderas, Susana Rocha

susana.rocha@kuleuven.be

## Highlights

FCLs are observed in different colorectal cancer (CRC) cell lines

FCLs are highly stable and persist for longer than 8 h at the plasma membrane

Detailed clathrin topology is quantified by PALM-TIRF super-resolution microscopy

FCLs are more prevalent in metastatic compared to poorly metastatic CRC cell lines

Cresens et al., iScience 26, 107327
August 18, 2023 
https://doi.org/10.1016/j.isci.2023.107327

iScience

CellPress
OPEN ACCESS

Article

# Flat clathrin lattices are linked to metastatic potential in colorectal cancer

Charlotte Cresens,[1] Guillermo Solís-Fernández,[1,2] Astha Tiwari,[1] Rik Nuyts,[1] Johan Hofkens,[1,3] Rodrigo Barderas,[2] and Susana Rocha[1,4,*]

## SUMMARY

**Clathrin assembles at the cells' plasma membrane in a multitude of clathrin-coated structures (CCSs). Among these are flat clathrin lattices (FCLs), alternative clathrin structures that have been found in specific cell types, including cancer cells. Here we show that these structures are also present in different colorectal cancer (CRC) cell lines, and that they are extremely stable with lifetimes longer than 8 h. By combining cell models representative of CRC metastasis with advanced fluorescence imaging and analysis, we discovered that the metastatic potential of CRC is associated with an aberrant membranous clathrin distribution, resulting in a higher prevalence of FCLs in cells with a higher metastatic potential. These findings suggest that clathrin organization might play an important yet unexplored role in cancer metastasis.**

## INTRODUCTION

Clathrin-mediated endocytosis (CME) is essential for the selective internalization of cell surface receptors in mammalian cells. The main actor in this process is clathrin, a triskelion-shaped protein consisting of three heavy and three light chains, which binds cargo molecules at the plasma membrane. Through the recruitment of additional triskelions, a honeycomb-like lattice consisting of hexagons and pentagons assembles. According to the CME model for *de novo* vesicle formation, this lattice can form a shallow invagination called clathrin-coated pit (CCP). Assisted by adaptor proteins, a CCP can bend further, increasing its curvature and the depth of the invagination, until a spherical clathrin-coated vesicle (CCV) is released into the intracellular environment.

In agreement with the general CME outline, a variety of clathrin-coated structures (CCSs) have been observed, ranging from nearly planar lattices or slightly curved CCPs to domed structures or highly curved CCVs.[1] However, alternative clathrin structures that do not fit this model have also been described, including flat clathrin lattices (FCLs, also termed clathrin plaques).[2–6] These structures are reported to be planar, heterogeneous and irregularly shaped non-classical CCSs that are too large to be resolved into a single diffraction-limited CCV.[2–6] FCLs are functional endocytic structures that can release CCVs,[4,7–9] but are more stable: while classical CCSs remain at the plasma membrane for about 30–90 s,[10–12] FCLs are significantly longer-lived, with reported lifetimes ranging from 2 to 10 min to more than 1 h.[5,6,13] FCLs have exclusively been found in specific cell types, including several cancer cell lines,[6,14] but a potential link between the presence of non-classical CCSs and cancer progression has not yet been investigated.

Previous research has shown that endocytosis is dysregulated in cancer[15–18] and that several proteins involved in CME are implicated in tumor cell migration, invasion, and metastasis.[19] By using subcellular proteomic analysis, we have previously established that proteins involved in vesicle trafficking, including in CME, are among the most dysregulated complexes in highly metastatic CRC cells compared to poorly metastatic CRC cells.[20,21]

In this work, we combined two isogenic cell models representative of CRC metastasis (KM12 and SW) with advanced fluorescence imaging to investigate whether cellular clathrin distribution is related to metastatic potential. The KM12 model consists of the poorly metastatic KM12C cell line obtained from a patient's primary CRC tumor, and the liver metastatic KM12SM and liver and lung metastatic KM12L4a cell lines, obtained through successive passages in nude mice.[22,23] The second model (namely SW) consists of the

[1]Molecular Imaging and Photonics Division, Chemistry Department, Faculty of Sciences, KU Leuven, Celestijnenlaan 200F, 3001 Heverlee, Belgium

[2]Chronic Disease Programme, UFIEC, Instituto de Salud Carlos III, 28220 Madrid, Spain

[3]Department of Molecular Spectroscopy, Max Planck Institute for Polymer Research, Ackermannweg 10, 55128 Mainz, Germany

[4]Lead contact

*Correspondence: susana.rocha@kuleuven.be

https://doi.org/10.1016/j.isci.2023.107327

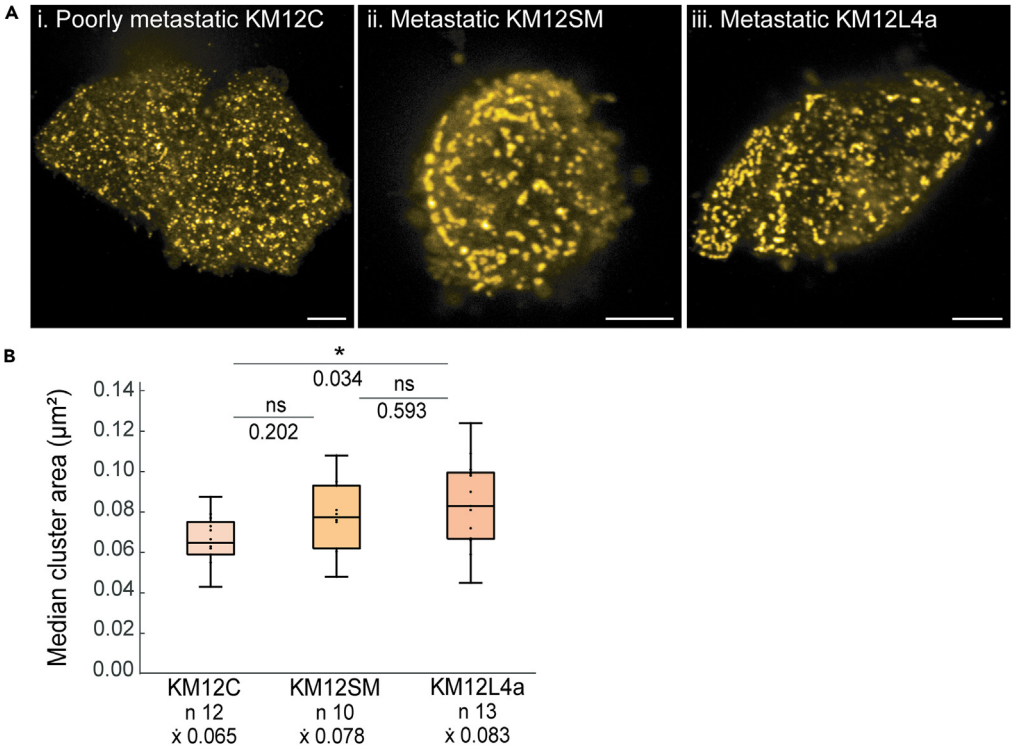


**Figure 1. Clathrin topology imaged with confocal fluorescence microscopy**

(A) Representative images of transiently transfected EYFP-CLTA visualized at the ventral plasma membrane (bottom, in contact with the glass coverslip) of poorly metastatic KM12C (i), metastatic KM12SM (ii), and metastatic KM12L4a (iii) CRC cells. Scale bars 5 µm.

(B) Median cluster area per cell, plotted per cell line. The number of datapoints (n, reflecting the number of cells), medians (x) and statistical significances (* significant difference for $p \leq 0.05$; ** significant difference for $p \leq 0.01$; *** significant difference for $p \leq 0.001$) are shown.

SW480 and SW620 pair of cell lines. The poorly metastatic SW480 cell line was obtained from a patient's primary CRC tumor and the metastatic SW620 cell line was derived from lymph node metastasis in the same patient.[24,25] Previous research reported a good correlation between findings in these cell models and patient samples,[21,26–32] indicating that they quite adequately mimic the different subtypes of CRC patients and the critical steps of CRC metastasis. We investigated clathrin organization and dynamics using standard confocal microscopy, and we quantified detailed clathrin topology using super-resolution PALM-TIRF microscopy and customized analysis algorithms. Our results show that extremely stable alternative CCSs, identified as FCLs, are far more prevalent in highly metastatic cells compared to their poorly metastatic counterparts. This suggests that aberrant clathrin organization could potentially be a key player in the process of cancer metastasis.

## RESULTS

### Stable FCLs are present in metastatic CRC cells

To investigate whether alternative CCSs are present in the KM12 cell model, we imaged the clathrin distribution at the ventral membrane of cells transiently transfected with clathrin light chain A (CLTA) fused to enhanced yellow fluorescent protein (EYFP-CLTA). Confocal images indicate that poorly and highly metastatic cells display remarkable differences in clathrin topology (Figure 1A). In the poorly metastatic KM12C cell line, clathrin predominantly appears as diffraction-limited dot-like structures, representing classical CCSs that fit the general CME model. In comparison, the two metastatic KM12SM and KM12L4a cell lines present an aberrant clathrin organization with both classical CCSs as well as larger, more elongated CCSs with longitudinal cross-sections reaching a few micrometers, which resemble FCLs. These differences were reflected in the median area of clathrin clusters in every cell. Specifically, metastatic KM12SM and KM12L4a cells exhibit a larger median cluster area compared to poorly metastatic KM12C cells (even though these

differences were not always significant, Figure 1B). Previous reports have shown that transient overexpression of the CLTA plasmid does not influence clathrin topology,[33] and our results support this finding since immunolabeling of endogenous clathrin heavy chain 1 (CLTC) resulted in a comparable topology (Figure S1).

To confirm that the observed elongated CCSs are indeed FCLs, we monitored clathrin dynamics in metastatic KM12SM cells for longer time intervals. As shown in Figure 2A and Video S1, classical dot-like CCSs are typically formed and internalized within 1–2 min, in line with their dynamic behavior during CME. In contrast, nearly all alternative CCSs remained present for longer periods of time and could still be observed after 8 h in both the metastatic KM12SM and KM12L4a cell lines (Figures 2B and 2C). Quantification of clathrin dynamics revealed that metastatic KM12SM cells have significantly more long-lived CCSs than their poorly metastatic KM12C counterparts (Figure 2D), and that these persistent CCSs are significantly larger than the short-lived clusters (Figure 2E), supporting our conclusion that these structures are FCLs. However, to the best of our knowledge, imaging of clathrin in FCLs for such prolonged periods of time has not yet been reported.

## Divergent clathrin topology can be quantified in single-molecule localization microscopy

To accurately quantify the distribution of clathrin and avoid erroneous interpretation of CCSs located closely to each other, we visualized clathrin topology (mEos3.2-CLTA) using PALM single-molecule localization microscopy (SMLM)[34,35] in TIRF-mode (Figures 3i–3ii). We selected total internal reflection (TIRF) illumination since it eliminates the background fluorescence signal from the cytoplasm, allowing for a more precise visualization of membrane-associated protein organization (Figure S2). Consistent with our confocal results, we detected predominantly classical CCSs in the poorly metastatic KM12C cells, and a mix of classical CCSs and alternative FCLs in the metastatic KM12 cells (Figures 4Ai–iii). Of note, variations were also observed between different cells of the same cell line, possibly reflecting differences in the biological status of cells (Figures S3A, S3B, and S4–S6 for full dataset). To quantify the apparent differences between poorly and highly metastatic cells, we developed a two-step analysis workflow to identify and classify clathrin clusters as classical CCSs or alternative FCLs (Figure 3), leveraging the single-molecule information content of the SMLM imaging strategy.

For cluster identification, we applied the density-based spatial clustering of applications with noise (DBSCAN) algorithm that is capable of detecting clusters in a noisy dataset without making assumptions about their shape or size.[36,37] After optimizing DBSCAN cluster parameters (MinPts and $\varepsilon$, Figure S9Aiii), and after discarding clusters with less than 50 localizations (corresponding to single clathrin molecules rather than a CCS, Figure S9B), the DBSCAN algorithm correctly identified individual clathrin clusters (Figure 3iii).

For cluster topology classification, different CCS characteristics such as cluster area, brightness, and roundness have previously been applied.[4,6,9,38,39] However, there seems to be a lack of unambiguous guidelines for parameter selection, so that different strategies rely on different CCS characteristics. We found that—besides cluster area, brightness, and roundness—two additional characteristics, namely cluster perimeter and the distance to the nearest neighboring cluster, were also effective in distinguishing between divergent CCSs (Figures S9C and S9D). Importantly, different clathrin topologies could not be distinguished based on a single characteristic in our dataset (Figure S10). Therefore, we designed a classification model that integrates multiple relevant CCS parameters to classify each cluster as a classical CCS or an alternative FCL (Figure 3iv). One advantage of our integrated model is that it can rely on a global threshold for the combined parameters, rather than relying on threshold values for the individual parameters for which a consensus seems to be lacking in the literature. We set the global threshold based on an internal reference determined for 1247 classical and 1042 alternative CCSs that were manually selected, ensuring that maximally 10% of the classical CCSs are misclassified. Using this automated analysis workflow (see STAR methods "PALM-TIRF cluster quantification" for more info) we can quickly, accurately, and objectively discriminate between classical and alternative clathrin topology in large SMLM datasets containing thousands of clusters (Figures 3iv–v).

To evaluate the effectiveness of our classification strategy, we examined the area of classified CCSs (Figure S9E), which is frequently used in the literature to identify alternative CCSs.[4,6,9,38,39] We found that the area of classical CCSs is cell-type independent for the KM12 cell model with an average area of

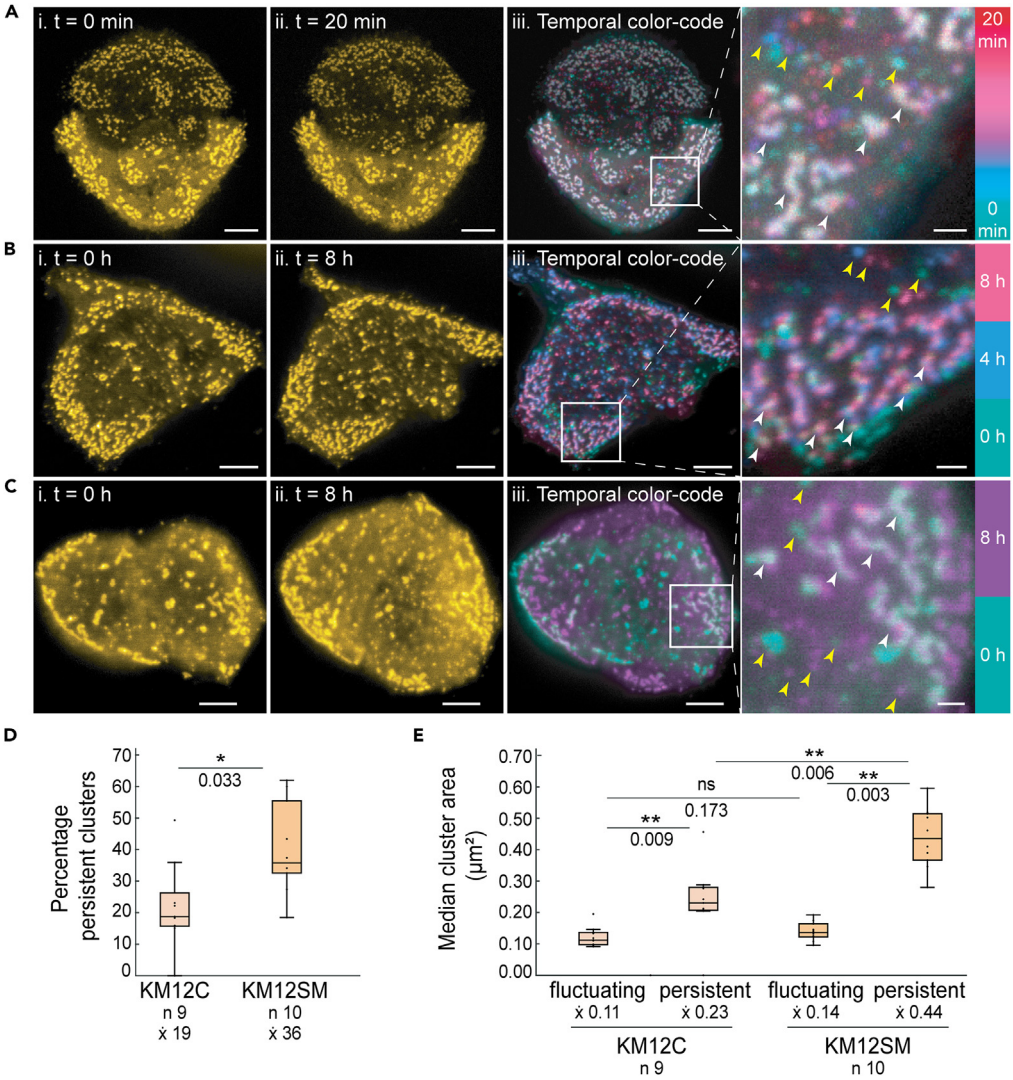


**Figure 2. Clathrin dynamics at the ventral membrane**

(A–C) Representative images of metastatic KM12SM (A and B) and metastatic KM12L4a (C) cells transiently transfected with EYFP-CLTA, imaged by time-lapse confocal microscopy for 20 min (A) or 8 h (B and C). First (i) and last (ii) timepoints of the time-lapse are shown, as well as the temporal color-coded image of the entire time-lapse (iii). For 8 h discontinuous measurements (B and C), the temporal color-code denotes the specific timepoints at which the cells were imaged. CCSs that were present for a limited amount of time, are shown in a single color from the color code (yellow arrows), while CCSs that were present for a longer time or persisted for the whole duration of the measurement are shown in the overlay color (white arrows). The overlay color can be either white if the structure remains for the entire duration, or can be the specific overlay color if it is detected in some specific timepoints (e.g., blue and pink). Scale bars 5 µm, except scale bars of enlargements 1 µm.

(D and E) Quantification of 20-min clathrin dynamics where the median percentage of persisting clusters per cell (D) and the median cluster area per cell (E) are plotted. The number of datapoints (n, reflecting the number of cells), medians (x) and statistical significances (* significant difference for $p \leq 0.05$; ** significant difference for $p \leq 0.01$; *** significant difference for $p \leq 0.001$) are shown.

$0.034 \pm 0.004\ \mu m^2$ (Mean $\pm$ standard deviation. Corresponding to a diameter of approximately $0.21 \pm 0.01\ \mu m$ when assuming a spherically shaped CCS). These results are in line with projections from the general CME model and with previous reports[4,6,9,39] considering that the resolution of optical microscopy yields slightly larger values compared to higher-resolution techniques like electron microscopy. In addition, we observed that alternative FCLs have an average area of $0.19 \pm 0.04\ \mu m^2$, which is in line with the >100 000 $nm^2$ benchmark reported by Grove et al.[6] and is on average 5.7 times larger than a classical

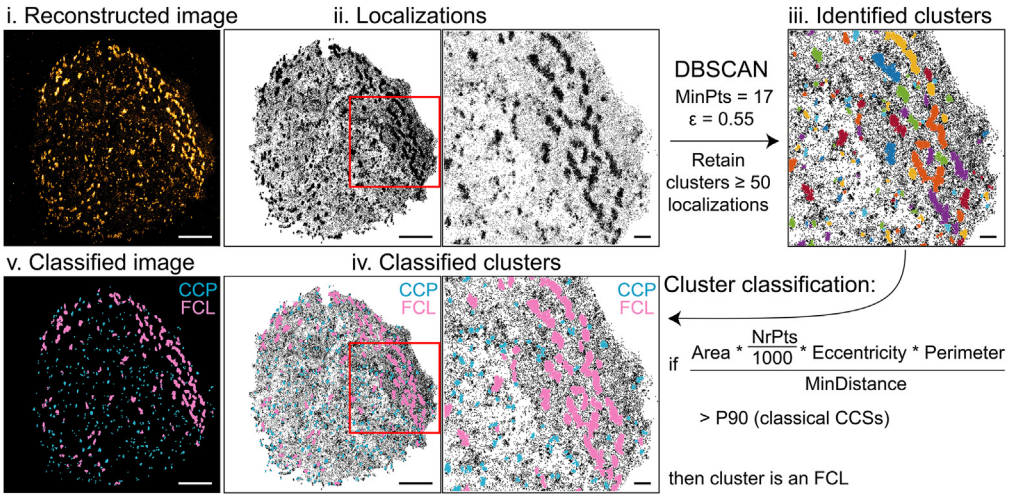


**Figure 3. Cluster identification and classification workflow illustrated in a metastatic KM12L4a cell**

Individual localizations (ii) that make up the PALM-TIRF image (i) were clustered using the DBSCAN algorithm with minimum 17 neighbors (MinPts) and search radius (ε) 0.55. Retaining clusters with ≥50 localizations resulted in identification of individual clathrin clusters (iii). The designed cluster classification model (iv and v) classifies these as either a classical CCS (blue, indicated as CCP) or an alternative FCL (pink) based on 5 cluster-specific parameters (cluster area, number of localizations NrPts, eccentricity, perimeter, and the distance to the nearest neighboring cluster MinDistance) and a global threshold. Scale bars 5 μm, except scale bars of enlargements 1 μm.

CCS. We also verified that cluster area is not correlated to cell area (Figure S9F). Overall, the similarities between our results and recent findings support our cluster classification model for the quantification of clathrin clusters in an SMLM dataset.

## FCLs are associated to metastatic potential in two different CRC models, as quantified with single-molecule localization microscopy

Having verified our analysis strategy, we quantified clathrin topology in the KM12 model by comparing the number of clusters classified as alternative FCLs with those classified as classical CCSs, where this ratio was calculated for each of the measured cells (Figure 4B). We found that within a given KM12 cell, there are more classical CCSs than alternative FCLs since the ratio is lower than 1. Importantly, this ratio is significantly higher for metastatic KM12 cells than for their poorly metastatic counterpart (Figure 4B). In addition, the significant difference between KM12SM and KM12L4a cells could be associated to their biologically different tropism, since KM12L4a cells are able to colonize the liver and lung in contrast to KM12SM cells that are only able to colonize the liver.[23] These results demonstrate that FCLs are associated with metastatic potential in the KM12 CRC model.

To reinforce our findings, we extended our research to the SW model for CRC metastasis. Clathrin topology imaged by PALM-TIRF microscopy is strikingly similar to that in the KM12 model, with predominantly small dot-like classical CCSs in the poorly metastatic SW480 cells, and a combination of classical CCSs and large, elongated FCLs in metastatic SW620 cells (Figures 4Aiv–v, S7, and S8 for full dataset). However, in the metastatic SW620 cells, clathrin seems to be reorganized even more extensively, since clathrin forms highly connected rosette-like structures that sometimes cover the entire ventral membrane with few classical CCSs present (Figure S3C). When applying our classification model to the SW dataset, we validated again that classical CCS area is cell-type independent (Figure S9E), and found that alternative FCLs are on average 6.1 times larger than classical CCSs (average area classical CCS 0.032 ± 0.005 $\mu m^2$, average area FCL 0.20 ± 0.08 $\mu m^2$). FCLs are significantly larger in the metastatic SW620 cell line compared to the poorly metastatic SW480 cell line (Figure S9E), and cluster area is again independent of cell area (Figure S9F). When quantifying clathrin topology in the SW model using the ratio of FCLs and classical CCSs (Figure 4B), we found that most cells have more classical CCSs than alternative FCLs and that the poorly metastatic cells of both cell models are not significantly different in this respect (Figure 4B). However, the metastatic SW620 cells have a significantly higher ratio when compared to their poorly metastatic

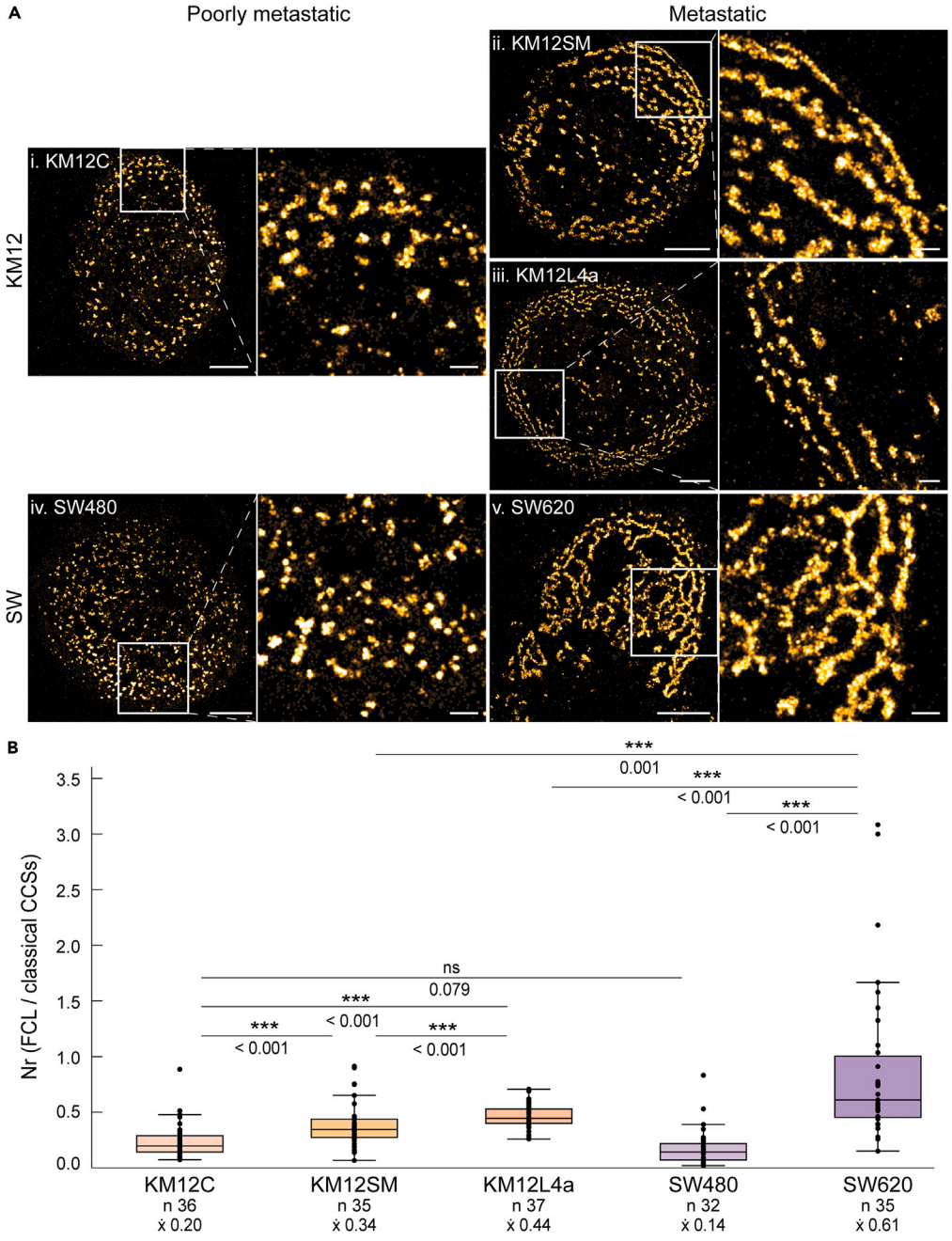


**Figure 4. Visualization and quantification of clathrin topology at the ventral membrane of poorly and highly metastatic cells of the KM12 and SW models**

(A) Representative PALM-TIRF images of clathrin (mEos3.2-CLTA) at the ventral membrane of the different cell lines are shown. Scale bars 5 μm, except scale bars of enlargements 1 μm.

(B) Quantification of clathrin topology using the ratio FCLs versus classical CCSs per cell. Note that most cells have more classical CCSs than alternative FCLs (ratio <1), except in 8 of the 35 SW620 cells. Data are plotted per cell line and the number of datapoints (n, reflecting the number of cells), medians (x) and statistical significances (* significant difference for $p \leq 0.05$; ** significant difference for $p \leq 0.01$; *** significant difference for $p \leq 0.001$; ns non-significant difference for $p > 0.05$) are shown.

counterpart (Figure 4B), demonstrating that FCLs may be associated with the metastatic potential of both KM12 and SW CRC cell models.

Since protein expression and cellular function are closely related, we set out to investigate whether the aberrant clathrin topology could be due to altered expression levels of certain CME actors. We quantified the expression of CLTA, CLTC, and AP2 subunit α2 (AP2A2, an adaptor protein involved in CME) in the KM12 and SW models via Western blot (Figure S11). When comparing poorly and highly metastatic cells within the same cell model, we found that AP2A2 expression is downregulated in metastatic SW cells, while it is highly upregulated in metastatic KM12 cells, the latter as previously reported for this cell model.[20] In terms of clathrin expression, we found that both CLTA and CLTC protein levels either remain unchanged or are downregulated in metastatic KM12 cells, while an opposite trend was seen within the SW model (CLTA is downregulated, but CLTC is upregulated in metastatic SW cells). Considering the differences between the KM12 and SW models, it is reasonable to assume that although alterations in CME actors might be inherent to CRCs' metastatic progression, the exact changes may be associated to the different tropism of the cancer cells. It is noteworthy that clathrin protein expression does not seem to cause the aberrant clathrin topology observed in these cell lines, as one might intuitively expect. In addition, our results indicate that besides protein expression levels there must be additional factors influencing clathrin topology that converge to a similar phenotype albeit via different molecular mechanisms.

## DISCUSSION

In this report, we show for the first time an association between metastatic potential and membranous clathrin distribution in two isogenic cell models representative of CRC metastasis. Confocal imaging revealed that poorly metastatic cells predominantly display classical dot-like CCSs, while metastatic cells exhibit both classical CCSs and larger, more elongated CCSs that we identified as FCLs based on their reported topology and lifetime. We observed FCLs for more than 8 h in our measurements, an extremely extended lifetime that has to the best of our knowledge not yet been reported. When quantifying detailed clathrin topology using advanced fluorescence microscopy, we found that FCLs can be detected in both highly and poorly metastatic CRC cells, but that they are far more prevalent in cells with a higher metastatic potential.

While there is a clear link between metastatic potential and aberrant clathrin organization, the cause of FCL formation in these cell models remains an enigma since our analysis could not pinpoint the divergent topology to the expression of a specific CME component. It was previously reported that both *AP2M1* expression levels and alternative splicing of CLTC can influence clathrin organization,[39,40] and therefore it could be that FCL formation cannot be attributed to one specific alteration. Instead, FCL formation may be cell type-specific or could depend on (interaction with) yet other proteins that were not analyzed here. For instance, there is growing evidence of an intimate relationship between FCLs and integrin αVβ5-containing reticular adhesions.[14,41–43] Alternatively, mechanobiological cues could play a role in FCL formation, since an altered plasma membrane tension[12] and certain properties of the extracellular environment like rigidity and presentation of adhesion ligands[12,38,43–46] were reported to affect the presence of alternative CCSs.

Given the role of FCLs as a platform for sustained receptor signaling and their connection to cell proliferation,[6,8,9,38] we hypothesize that alternative clathrin organization might be involved in cancer progression and metastasis. In addition, considering their close association with integrins and the extracellular matrix, these structures may be relevant to the migration of metastatic cancer cells during tumor dissemination. Further investigation of the link between metastatic potential and aberrant clathrin organization will contribute to unraveling the function of clathrin in tumor biology.

### Limitations of the study

While this study reveals an association between metastatic potential and aberrant clathrin distribution, it is important to acknowledge some inherent limitations. Firstly, while our quantitative analysis establishes a correlation between aberrant clathrin organization and metastatic potential in two CRC models, the study does not establish causality. The precise relationship between clathrin organization and metastatic potential remains uncertain, including whether clathrin organization is a consequence of metastatic potential, involved in acquiring metastatic traits, or unrelated. Additional studies incorporating functional experiments and perturbation techniques are warranted to manipulate clathrin organization and assess its impact on metastatic behavior. Secondly, while the cell models used in this exhibit a high degree of correlation with patient samples, it is important to acknowledge that the 2-dimensional arrangement of cultured cells

may not fully replicate the complex *in vivo* situation, where cell-cell and cell-matrix interactions influence both biochemical and mechanobiological cell responses. Additional studies using models that better mimic the *in vivo* situation would contribute to a more comprehensive understanding of the prevalence and potential role of aberrant clathrin organization in cancer progression and metastasis.

## STAR★METHODS

Detailed methods are provided in the online version of this paper and include the following:

- KEY RESOURCES TABLE
- RESOURCE AVAILABILITY
  - Lead contact
  - Materials availability
  - Data and code availability
- EXPERIMENTAL MODEL AND STUDY PARTICIPANT DETAILS
- METHOD DETAILS
  - Colorectal cancer cell culture
  - Western blot and quantification
  - Plasmids and transfection
  - Immunolabeling
  - Confocal fluorescence microscopy
  - Confocal clathrin topology
  - Confocal clathrin dynamics
  - PALM-TIRF fluorescence microscopy
  - PALM-TIRF cluster quantification
- QUANTIFICATION AND STATISTICAL ANALYSIS

## SUPPLEMENTAL INFORMATION

Supplemental information can be found online at https://doi.org/10.1016/j.isci.2023.107327.

## ACKNOWLEDGMENTS

The authors would like to thank colleagues from KU Leuven MIP division, especially from the group of Prof. Rocha, for their input and critical questions. We thank Fidler's lab (MD Anderson Cancer Center) for sharing KM12 model cell lines and Dr. Zhuang for making the EYFP-CLTA plasmid available (Addgene plasmid # 20921). We also thank Prof. R. Vitale (Université de Lille) for guidance and feedback on the statistical analysis. This work was funded by the Research Foundation - Flanders (C.C. is recipient of a PhD fellowship for fundamental research, FWO grant number 1121221N. G.S.-F. is recipient of a predoctoral contract, FWO grant number 1193818N), and the AES-ISCIII program to R.B. (PI17CIII/00045 and PI20CIII/00019 grants partially supported by FEDER funds). J.H. acknowledges financial support from the Research Foundation Flanders (FWO grant numbers G0C1821N and ZW15 09-G0H6316N), from the Flemish Government through long-term structural funding Methusalem (CASAS2, Meth/15/04), and from the MPI as a fellow. S.R. acknowledges financial support from KU Leuven (grant numbers KA/20/026 and IDN/20/021).

## AUTHOR CONTRIBUTIONS

C.C. and A.T. performed the optical imaging experiments and analyzed the data. Quantification of protein expression was performed by G.S.-F. and C.C. R.N. assisted with the acquisition of images using the confocal microscope. S.R. and C.C. designed the experiments and wrote the final manuscript, with input from all the co-authors. J.H., R.B., and S.R. supervised the work.

## DECLARATION OF INTERESTS

The authors declare no competing interests.

Received: April 4, 2023
Revised: June 9, 2023
Accepted: July 5, 2023
Published: July 12, 2023

## REFERENCES


1. Sochacki, K.A., and Taraska, J.W. (2019). From flat to curved clathrin: controlling a plastic ratchet. Trends Cell Biol. *29*, 241–256. https://doi.org/10.1016/j.tcb.2018.12.002.

2. Heuser, J., and Evans, L. (1980). Three-dimensional visualization of coated vesicle formation in fibroblasts. J. Cell Biol. *84*, 560–583. https://doi.org/10.1083/jcb.84.3.560.

3. Engqvist-Goldstein, A.E.Y., Zhang, C.X., Carreno, S., Barroso, C., Heuser, J.E., and Drubin, D.G. (2004). RNAi-mediated Hip1R silencing results in stable association between the endocytic machinery and the actin assembly machinery. Mol. Biol. Cell *15*, 1666–1679. https://doi.org/10.1091/mbc.E03.

4. Merrifield, C.J., Perrais, D., and Zenisek, D. (2005). Coupling between clathrin-coated-pit invagination, cortactin recruitment, and membrane scission observed in live cells. Cell *121*, 593–606. https://doi.org/10.1016/j.cell.2005.03.015.

5. Saffarian, S., Cocucci, E., and Kirchhausen, T. (2009). Distinct dynamics of endocytic clathrin-coated pits and coated plaques. PLoS Biol. *7*, 10001911–e1000218. https://doi.org/10.1371/journal.pbio.1000191.

6. Grove, J., Metcalf, D.J., Knight, A.E., Wavre-Shapton, S.T., Sun, T., Protonotarios, E.D., Griffin, L.D., Lippincott-Schwartz, J., and Marsh, M. (2014). Flat clathrin lattices: stable features of the plasma membrane. Mol. Biol. Cell *25*, 3581–3594. https://doi.org/10.1091/mbc.E14-06-1154.

7. Taylor, M.J., Perrais, D., and Merrifield, C.J. (2011). A high precision survey of the molecular dynamics of mammalian clathrin-mediated endocytosis. PLoS Biol. *9*, e1000604–e1000623. https://doi.org/10.1371/journal.pbio.1000604.

8. Lampe, M., Pierre, F., Al-Sabah, S., Krasel, C., and Merrifield, C.J. (2014). Dual single-scission event analysis of constitutive transferrin receptor (TfR) endocytosis and ligand-triggered β2-adrenergic receptor (β2AR) or Mu-opioid receptor (MOR) endocytosis. Mol. Biol. Cell *25*, 3070–3080. https://doi.org/10.1091/mbc.E14-06-1112.

9. Leyton-Puig, D., Isogai, T., Argenzio, E., Van Den Broek, B., Klarenbeek, J., Janssen, H., Jalink, K., and Innocenti, M. (2017). Flat clathrin lattices are dynamic actin-controlled hubs for clathrin-mediated endocytosis and signalling of specific receptors. Nat. Commun. *8*, 16068–16114. https://doi.org/10.1038/ncomms16068.

10. Ehrlich, M., Boll, W., Van Oijen, A., Hariharan, R., Chandran, K., Nibert, M.L., and Kirchhausen, T. (2004). Endocytosis by random initiation and stabilization of clathrin-coated pits. Cell *118*, 591–605. https://doi.org/10.1016/j.cell.2004.08.017.

11. Loerke, D., Mettlen, M., Yarar, D., Jaqaman, K., Jaqaman, H., Danuser, G., and Schmid, S.L. (2009). Cargo and dynamin regulate clathrin-coated pit maturation. PLoS Biol. *7*, e57–e0639. https://doi.org/10.1371/journal.pbio.1000057.

12. Baschieri, F., Porshneva, K., and Montagnac, G. (2020). Frustrated clathrin-mediated endocytosis – causes and possible functions. J. Cell Sci. *133*, jcs240861. https://doi.org/10.1242/jcs.240861.

13. Lampe, M., Vassilopoulos, S., and Merrifield, C. (2016). Clathrin coated pits, plaques and adhesion. J. Struct. Biol. *196*, 48–56. https://doi.org/10.1016/j.jsb.2016.07.009.

14. Zuidema, A., Wang, W., Kreft, M., Bleijerveld, O.B., Hoekman, L., Aretz, J., Böttcher, R.T., Fässler, R., and Sonnenberg, A. (2022). Molecular determinants of αVβ5 localization in flat clathrin lattices – role of αVβ5 in cell adhesion and proliferation. J. Cell Sci. *135*, jcs259465. https://doi.org/10.1242/jcs.259465.

15. Ramsay, A.G., Marshall, J.F., and Hart, I.R. (2007). Integrin trafficking and its role in cancer metastasis. Cancer Metastasis Rev. *26*, 567–578. https://doi.org/10.1007/s10555-007-9078-7.

16. Lanzetti, L., and Di Fiore, P.P. (2008). Endocytosis and cancer: an "insider" network with dangerous liaisons. Traffic *9*, 2011–2021. https://doi.org/10.1111/j.1600-0854.2008.00816.x.

17. Mosesson, Y., Mills, G.B., and Yarden, Y. (2008). Derailed endocytosis: an emerging feature of cancer. Nat. Rev. Cancer *8*, 835–850. https://doi.org/10.1038/nrc2521.

18. Elkin, S.R., Bendris, N., Reis, C.R., Zhou, Y., Xie, Y., Huffman, K.E., Minna, J.D., and Schmid, S.L. (2015). A systematic analysis reveals heterogeneous changes in the endocytic activities of cancer cells. Cancer Res. *75*, 4640–4650. https://doi.org/10.1158/0008-5472.CAN-15-0939.

19. Khan, I., and Steeg, P.S. (2021). Endocytosis: a pivotal pathway for regulating metastasis. Br. J. Cancer *124*, 66–75. https://doi.org/10.1038/s41416-020-01179-8.

20. Mendes, M., Peláez-García, A., López-Lucendo, M., Bartolomé, R.A., Calviño, E., Barderas, R., and Casal, J.I. (2017). Mapping the spatial proteome of metastatic cells in colorectal cancer. Proteomics *17*, 1–11. https://doi.org/10.1002/pmic.201700094.

21. Solís-Fernández, G., Montero-Calle, A., Martínez-Useros, J., López-Janeiro, Á., Ríos, V.D.L., Sanz, R., Dziakova, J., Milagrosa, E., Fernández-Aceñero, M.J., Peláez-García, A., et al. (2022). Spatial Proteomic Analysis of Isogenic Metastatic Colorectal Cancer Cells Reveals Key Dysregulated Proteins Associated with Lymph Node, Liver, and Lung Metastasis. Cells *11*, 1–23. https://doi.org/10.3390/cells11030447.

22. Morikawa, K., Walker, S.M., Jessup, J.M., and Fidler, I.J. (1988). In vivo selection of highly metastatic cells from surgical specimens of different primary human colon carcinomas implanted into nude mice. Cancer Res. *48*, 1943–1948.

23. Morikawa, K., Walker, S.M., Nakajima, M., Pathak, S., Jessup, J.M., and Fidler, I.J. (1988). Influence of organ environment on the growth, selection, and metastasis of human colon carcinoma cells in nude mice. Cancer Res. *48*, 6863–6871.

24. Leibovitz, A., Stinson, J.C., McCombs, W.B., McCoy, C.E., Mazur, K.C., and Mabry, N.D. (1976). Classification of Human Colorectal Adenocarcinoma Cell Lines. Cancer Res. *36*, 4562–4569.

25. Hewitt, R.E., McMarlin, A., Kleiner, D., Wersto, R., Martin, P., Tsoskas, M., Stamp, G.W.H., and Stetler-Stevenson, W.G. (2000). Validation of a model of colon cancer progression. J. Pathol. *192*, 446–454. https://doi.org/10.1002/1096-9896(2000)9999:9999<::AID-PATH775>3.0.CO;2-K.

26. Hegde, P., Qi, R., Gaspard, R., Abernathy, K., Dharap, S., Earle-Hughes, J., Gay, C., Nwokekeh, N.U., Chen, T., Saeed, A.I., et al. (2001). Identification of tumor markers in models of human colorectal cancer using a 19,200-element complementary DNA microarray. Cancer Res. *61*, 7792–7797.

27. Kuniyasu, H., Ohmori, H., Sasaki, T., Sasahira, T., Yoshida, K., Kitadai, Y., and Fidler, I.J. (2003). Production of Interleukin 15 by Human Colon Cancer Cells Is Associated with Induction of Mucosal Hyperplasia, Angiogenesis, and Metastasis. Clin. Cancer Res. *9*, 4802–4810.

28. Li, A., Varney, M.L., and Singh, R.K. (2004). Constitutive expression of growth regulated oncogene (gro) in human colon carcinoma cells with different metastatic potential and its role in regulating their metastatic phenotype. Clin. Exp. Metastasis *21*, 571–579. https://doi.org/10.1007/s10585-004-5458-3.

29. Barderas, R., Bartolomé, R.A., Fernandez-Aceñero, M.J., Torres, S., and Casal, J.I. (2012). High expression of IL-13 receptor α2 in colorectal cancer is associated with invasion, liver metastasis, and poor prognosis. Cancer Res. *72*, 2780–2790. https://doi.org/10.1158/0008-5472.CAN-11-4090.

30. Calon, A., Espinet, E., Palomo-Ponce, S., Tauriello, D.V.F., Iglesias, M., Céspedes, M.V., Sevillano, M., Nadal, C., Jung, P., Zhang, X.H.F., et al. (2012). Dependency of Colorectal Cancer on a TGF-β-Driven Program in Stromal Cells for Metastasis Initiation. Cancer Cell *22*, 571–584. https://doi.org/10.1016/j.ccr.2012.08.013.

31. Solís-Fernández, G., Montero-Calle, A., Sánchez-Martínez, M., Peláez-García, A., Fernández-Aceñero, M.J., Pallarés, P., Alonso-Navarro, M., Mendiola, M., Hendrix, J., Hardisson, D., et al. (2022). Aryl hydrocarbon receptor-interacting protein regulates tumorigenic and metastatic properties of colorectal cancer cells driving liver metastasis. Br. J. Cancer *136*, 1604–1615. https://doi.org/10.1038/s41416-022-01762-1.

32. Montero-Calle, A., Gómez de Cedrón, M., Quijada-Freire, A., Solís-Fernández, G., López-Alonso, V., Espinosa-Salinas, I., Peláez-García, A., Fernández-Aceñero, M.J., Ramírez

de Molina, A., and Barderas, R. (2022). Metabolic Reprogramming Helps to Define Different Metastatic Tropisms in Colorectal Cancer. Front. Oncol. *12*, 1–19. https://doi.org/10.3389/fonc.2022.903033.

33. Gaidarov, I., Santini, F., Warren, R.A., and Keen, J.H. (1999). Spatial control of coated-pit dynamics in living cells. Nat. Cell Biol. *1*, 1–7. https://doi.org/10.1038/8971.

34. Betzig, E., Patterson, G.H., Sougrat, R., Lindwasser, O.W., Olenych, S., Bonifacino, J.S., Davidson, M.W., Lippincott-Schwartz, J., and Hess, H.F. (2006). Imaging intracellular fluorescent proteins at nanometer resolution. Science *313*, 1642–1645. https://doi.org/10.1126/science.1127344.

35. Hess, S.T., Girirajan, T.P.K., and Mason, M.D. (2006). Ultra-high resolution imaging by fluorescence photoactivation localization microscopy. Biophys. J. *91*, 4258–4272. https://doi.org/10.1529/biophysj.106.091116.

36. Ester, M., Kriegel, H.-P., Sander, J., and Xu, X. (1996). A density-based algorithm for discovering clusters in large spatial databases with noise. KDD-96 Proc. 226–231. https://doi.org/10.1016/B978-044452701-1.00067-3.

37. Khater, I.M., Nabi, I.R., and Hamarneh, G. (2020). A Review of Super-Resolution Single-Molecule Localization Microscopy Cluster Analysis and Quantification Methods. Patterns *1*, 100038. https://doi.org/10.1016/j.patter.2020.100038.

38. Baschieri, F., Dayot, S., Elkhatib, N., Ly, N., Capmany, A., Schauer, K., Betz, T., Vignjevic, D.M., Poincloux, R., and Montagnac, G. (2018). Frustrated endocytosis controls contractility-independent mechanotransduction at clathrin-coated structures. Nat. Commun. *9*, 3825–3913. https://doi.org/10.1038/s41467-018-06367-y.

39. Moulay, G., Lainé, J., Lemaitre, M., Nakamori, M., Nishino, I., Caillol, G., Mamchaoui, K., Julien, L., Dingli, F., Loew, D., et al. (2020). Alternative splicing of clathrin heavy chain contributes to the switch from coated pits to plaques. J. Cell Biol. *219*, 1–16. https://doi.org/10.1083/jcb.201912061.

40. Dambournet, D., Sochacki, K.A., Cheng, A.T., Akamatsu, M., Taraska, J.W., Hockemeyer, D., and Drubin, D.G. (2018). Genome-edited human stem cells expressing fluorescently labeled endocytic markers allow quantitative analysis of clathrin-mediated endocytosis during differentiation. J. Cell Biol. *217*, 3301–3311. https://doi.org/10.1083/jcb.201710084.

41. Lock, J.G., Jones, M.C., Askari, J.A., Gong, X., Oddone, A., Olofsson, H., Göransson, S., Lakadamyali, M., Humphries, M.J., and Strömblad, S. (2018). Reticular adhesions are a distinct class of cell-matrix adhesions that mediate attachment during mitosis. Nat. Cell Biol. *20*, 1290–1302. https://doi.org/10.1038/s41556-018-0220-2.

42. Lock, J.G., Baschieri, F., Jones, M.C., Humphries, J.D., Montagnac, G., Strömblad, S., and Humphries, M.J. (2019). Clathrin-containing adhesion complexes. J. Cell Biol. *218*, 2086–2095. https://doi.org/10.1083/jcb.201811160.

43. Hakanpää, L., Abouelezz, A., Lenaerts, A., Culfa, S., Algie, M., Bärlund, J., Katajisto, P., Mcmahon, H., and Almeida-souza, L. (2023). Reticular adhesions are assembled at flat clathrin lattices and opposed by active integrin α5β1. J. Cell Biol. *222*. https://doi.org/10.1083/jcb.202303107.

44. Elkhatib, N., Bresteau, E., Baschieri, F., Rioja, A.L., Van Niel, G., Vassilopoulos, S., and Montagnac, G. (2017). Tubular clathrin/AP-2 lattices pinch collagen fibers to support 3D cell migration. Science *356*, eaal4713. https://doi.org/10.1126/science.aal4713.

45. Zuidema, A., Wang, W., Kreft, M., Te Molder, L., Hoekman, L., Bleijerveld, O.B., Nahidiazar, L., Janssen, H., and Sonnenberg, A. (2018). Mechanisms of integrin αVβ5 clustering in flat clathrin lattices. J. Cell Sci. *131*, jcs221317. https://doi.org/10.1242/jcs.221317.

46. Bresteau, E., Elkhatib, N., Baschieri, F., Bellec, K., Guérin, M., and Montagnac, G. (2021). Clathrin-coated structures support 3D directed migration through local force transmission. Sci. Adv. *7*, eabf4647. https://doi.org/10.1126/sciadv.abf4647.

47. Wiśniewski, J.R., and Gaugaz, F.Z. (2015). Fast and sensitive total protein and peptide assays for proteomic analysis. Anal. Chem. *87*, 4110–4116. https://doi.org/10.1021/ac504689z.

48. Abràmoff, M.D., Magalhães, P.J., and Ram, S.J. (2004). Image processing with imageJ. Biophotonics Int *11*, 36–41.

49. Schneider, C.A., Rasband, W.S., and Eliceiri, K.W. (2012). NIH Image to ImageJ: 25 years of image analysis. Nat. Methods *9*, 671–675. https://doi.org/10.1038/nmeth.2089.

50. Rust, M.J., Lakadamyali, M., Zhang, F., and Zhuang, X. (2004). Assembly of endocytic machinery around individual influenza viruses during viral entry. Nat. Struct. Mol. Biol. *11*, 567–573. https://doi.org/10.1038/nsmb769.

51. Arganda-Carreras, I., Kaynig, V., Rueden, C., Eliceiri, K.W., Schindelin, J., Cardona, A., and Sebastian Seung, H. (2017). Trainable Weka Segmentation: A machine learning tool for microscopy pixel classification. Bioinformatics *33*, 2424–2426. https://doi.org/10.1093/bioinformatics/btx180.

52. Postma, M., and Goedhart, J. (2019). Plotsofdata—a web app for visualizing data together with their summaries. PLoS Biol. *17*, e3000202. https://doi.org/10.1371/journal.pbio.3000202.

53. Hooton, J.W. (1991). Randomization tests: statistics for experimenters. Comput. Methods Progr. Biomed. *35*, 43–51. https://doi.org/10.1016/0169-2607(91)90103-Z.

54. Rocha, S., De Keersmaecker, H., Uji-i, H., Hofkens, J., and Mizuno, H. (2014). Photoswitchable fluorescent proteins for superresolution fluorescence microscopy circumventing the diffraction limit of light. In Fluorescence Spectroscopy and Microscopy. Methods in Molecular Biology, *1076*, Y. Engelborghs and A. Visser, eds. (Humana Press). https://doi.org/10.1007/978-1-62703-649-8_36.

55. Dedecker, P., Duwé, S., Neely, R.K., and Zhang, J. (2012). Localizer: fast, accurate, open-source, and modular software package for superresolution microscopy. J. Biomed. Opt. *17*, 126008–126011. https://doi.org/10.1117/1.JBO.17.12.

56. Moshtagh, N. (2022). Minimum Volume Enclosing Ellipsoid. https://www.mathworks.com/matlabcentral/fileexchange/9542-minimum-volume-enclosing-ellipsoid.

## STAR★METHODS

### KEY RESOURCES TABLE

| REAGENT or RESOURCE | SOURCE | IDENTIFIER |
|---|---|---|
| **Antibodies** | | |
| rabbit anti-CLTA | Proteintech | 10852-1-AP<br>RRID:AB_2083025 |
| mouse anti-CLTC | Proteintech | 66487-1-Ig<br>RRID:AB_2881852 |
| mouse anti-AP2A2 | Santa cruz | sc-55497<br>RRID:AB_2056344 |
| mouse anti-Rho GDI | Santa cruz | sc-373724<br>RRID:AB_10917570 |
| goat anti-rabbit (GAR)-HRP conjugate | Sigma | A6154<br>RRID:AB_258284 |
| goat anti-mouse (GAM)-HRP conjugate | Sigma | A4416<br>RRID:AB_258167 |
| mouse anti-CLTC | NovusBio | NB300-613<br>RRID:AB_10130252 |
| goat anti-mouse (GAM)-Atto647N | Sigma | 50185<br>RRID:AB_1137661 |
| **Chemicals, peptides, and recombinant proteins** | | |
| ECL Pico PLUS Chemiluminescent Substrate | Thermo, 34580 | N/A |
| TransIT-X2® | Mirus, 6000 | N/A |
| FuGENE® 6 | Promega, E2691 | N/A |
| **Experimental models: Cell lines** | | |
| KM12C cell line | Fidler's lab (MD Anderson Cancer Center) | RRID:CVCL_9547 |
| KM12SM cell line | Fidler's lab (MD Anderson Cancer Center) | RRID:CVCL_9548 |
| KM12L4a cell line | Fidler's lab (MD Anderson Cancer Center) | RRID:CVCL_W220 |
| SW480 cell line | ATCC, CCL-228 | RRID:CVCL_0546 |
| SW620 cell line | ATCC, CCL-227 | RRID:CVCL_0547 |
| **Recombinant DNA** | | |
| EYFP-CLTA | Addgene | Addgene_20921 |
| mEos3.2-CLTA | This manuscript | N/A |
| **Software and algorithms** | | |
| ImageJ 1.53c | Abràmoff et al.[48]<br>Schneider et al.[49] | https://imagej.nih.gov/ij/ |
| MATLAB R2022a | MathWorks | https://nl.mathworks.com/store |
| Publicly available MATLAB Localizer function | Dedecker et al.[55] | https://bitbucket.org/pdedecker/localizer/src/master/ |
| Publicly available MATLAB MinVolEllipse function | Nima Moshtagh et al.[56] | https://www.mathworks.com/matlabcentral/fileexchange/9542-minimum-volume-enclosing-ellipsoid |
| Custom-written MATLAB analysis algorithm MATLAB_CODE_Localizations_bulk | This manuscript | https://zenodo.org/record/8082373 |

(*Continued on next page*)

*Continued*

| REAGENT or RESOURCE | SOURCE | IDENTIFIER |
|---|---|---|
| Custom-written MATLAB analysis algorithm MATLAB_CODE_DBSCAN_and_cluster_properties_bulk | This manuscript | https://zenodo.org/record/8082373 |
| Custom-written MATLAB analysis algorithm MATLAB_CODE_cluster_classification_bulk | This manuscript | https://zenodo.org/record/8082373 |
| Custom-written MATLAB analysis algorithm get_prop_clusters | This manuscript | https://zenodo.org/record/8082373 |
| Huygens Professional version 19.10 | Scientific Volume Imaging B.V. | https://svi.nl/Download |
| PlotsOfDifferences web app | Goedhart et al.[52] Hooton et al.[53] | https://huygens.science.uva.nl/PlotsOfDifferences/ |
| Others | | |
| WB image developer: Amersham Imager 680 | GE Healthcare | N/A |
| Leica TCS SP8 confocal microscope with temperature and CO2 control, and 63x water or 63× oil objective | Leica Microsystems GmbH | N/A |
| Homebuilt PALM-TIRF fluorescence microscope | Rocha et al.[54] | N/A |

## RESOURCE AVAILABILITY

### Lead contact

Further information and requests for resources and reagents should be directed to Prof. Dr. Susana Rocha (susana.rocha@kuleuven.be).

### Materials availability

This study generated the new unique mEos3.2-CLTA plasmid, produced by replacing the EYFP coding sequence of EYFP-CLTA (generated by Xiaowei Zhuang, Addgene plasmid EYFP Clathrin, # 20921) by mEos3.2 using standard molecular cloning techniques. This plasmid is available upon reasonable request to the lead contact.

### Data and code availability

- Data: All data reported in this paper will be shared by the lead contact upon request.
- Code: All original code has been deposited at Zenodo and is publicly available as of the date of publication. DOIs are listed in the key resources table.
- Any additional information required to reanalyze the data reported in this paper is available from the lead contact upon request.

## EXPERIMENTAL MODEL AND STUDY PARTICIPANT DETAILS

Experimental models used in this study were isogenic KM12C, KM12SM and KM12L4a cell lines from Fidler's lab (MD Anderson Cancer Center) and isogenic SW480 and SW620 cell lines from ATCC (American Type Culture Collection).

The KM12 model consists of the poorly metastatic KM12C cell line obtained from a patients' primary CRC tumor, and the liver metastatic KM12SM and liver and lung metastatic KM12L4a cell lines were obtained through successive passages in nude mice. The sex or age of the patients from which these cell lines are derived are unknown, since they are not reported in the literature. The second model (namely SW) consists of the SW480 and SW620 pair of cell lines. The poorly metastatic SW480 cell line was obtained from the primary CRC tumor of a 50-year-old male patient and the metastatic SW620 cell line was derived from lymph node metastasis in the same patient.[24,25]

Cell lines were maintained in a humidified incubator at 37°C and 5% CO2 in Dulbecco's Modified Eagle Medium (DMEM, Gibco, 31053028) supplemented with 10% Fetal Bovine Serum (FBS, Sigma, F7524), 1%

GlutaMAX (Gibco, 35050038) and 0.1% Gentamycin (Carl Roth, 2475.1). Cell lines were tested and found negative for mycoplasma contamination.

## METHOD DETAILS

### Colorectal cancer cell culture

Isogenic KM12C, KM12SM and KM12L4a cell lines from Fidler's lab (MD Anderson Cancer Center) and isogenic SW480 and SW620 cell lines from ATCC (American Type Culture Collection) were used.[22,23] Cell lines were maintained in a humidified incubator at 37°C and 5% $CO_2$ in Dulbecco's Modified Eagle Medium (DMEM, Gibco, 31053028) supplemented with 10% FBS (Sigma, F7524), 1% GlutaMAX (Gibco, 35050038) and 0.1% Gentamycin (Carl Roth, 2475.1).

### Western blot and quantification

Cells grown to 90% confluence were harvested using 1x Trypsin-EDTA (Thermo, 59418C), pelleted by centrifugation (5 min at 220 G) and the dry pellet was frozen at −20°C for at least 1 h. Protein extracts were obtained by cell lysis using RIPA buffer mixed with phosphatases and proteases inhibitor cocktails (RIPA Sigma, R0278 with 1/100 phosphatase inhibitor MCE, HY-K0022 and 1/100 protease inhibitor MCE, HY-K0010) and 10 min centrifugation at 21 000 G. Next, 5 μg protein extracts quantified using the Tryptophan fluorescence method[21,47] were separated on a 10% SDS-PAGE gel alongside a PageRuler Plus Prestained Protein Ladder 10 to 250 kDa (Thermo, 26619) under reducing conditions and transferred onto a nitrocellulose membrane for 90 min at 100 V. Protein transfer was verified by Ponceau staining (Sigma, P3504) which was afterward removed by washes with DPBST (DPBS Thermo, 14200067 + 0.1% Tween 20 Sigma, P1379). For specific target detection, the membrane was cut according to the expected band sizes, blocked in blocking buffer (3% skimmed milk in DPBST) for 1 h at room temperature, and incubated with primary antibody diluted in blocking buffer overnight at 4°C. The membrane was washed 3x with DPBST for 10 min and incubated for 1 h at room temperature with secondary antibody diluted in blocking buffer. Washes were performed as before, chemiluminescent signal was generated with the ECL Pico PLUS Chemiluminescent Substrate (Thermo, 34580) and protein bands were imaged on an Amersham Imager 680 (GE Healthcare). Details of the antibodies used are listed in Table S1. For quantification, standard densitometry was performed using the ImageJ gel analysis tool.[48,49] The peak area was measured in the lane plot and numerical values were further processed in Excel, normalized using Rho GDI signal as loading control, and referenced to the poorly metastatic cell line of the corresponding cell model for their comparison.

### Plasmids and transfection

Plasmids for transient expression of CLTA were EYFP-CLTA (generated by Xiaowei Zhuang, Addgene plasmid EYFP-Clathrin, # 20921),[50] and mEos3.2-CLTA, generated by replacing the EYFP coding sequence by mEos3.2 using standard molecular cloning techniques. Reverse transfections were performed immediately after seeding the appropriate number of cells (Table S1) in a 35 mm disk with 14 mm glass-bottom insert (Cellvis, D35-14-1.5-N), a glass-bottom 6-well plate (Cellvis, P06-1.5H-N) or a 35 mm disk with imprinted grid (Ibidi, 80156). The transfection mixture for EYFP-CLTA was prepared using TransIT-X2 (Mirus, 6000) according to the Universal Transfection Reagent Protocol by Sigma-Aldrich (Sigma, T0956) with optimized reagent quantities (Table S1). Briefly, plasmid DNA was added to 50 μL DMEM with 1% GlutaMAX in a first tube (A), while TransIT-X2 was added to 50 μL DMEM with 1% GlutaMAX in a second tube (B). Both tubes were gently vortexed, tube B was immediately added to tube A, gently vortexed and spun down. The transfection mixture for mEos3.2-CLTA was prepared by first adding FuGENE 6 (Promega, E2691) and then plasmid DNA to 100 μL DMEM with 1% GlutaMAX. For both methods the transfection mixture was added dropwise to recently seeded cells after 15–20 min incubation at room temperature, and the sample was incubated in a humidified incubator at 37°C and 5% $CO_2$ for the appropriate time (Table S1).

### Immunolabeling

Immunolabeling of CLTC was performed on EYFP-CLTA transfected samples in a 35 mm disk. Samples were washed 1x with 1 mL prewarmed DPBS (Thermo, 14200067), fixed for 10 min in 200 μL prewarmed PFA 4% (Thermo, 28908) in DPBS, then washed 3x with 1 mL DPBST (DPBS +0.1% Tween 20 Sigma, P1379) and permeabilized with 200 μL 0.1% Triton X-100 (Sigma, 9002-93-1) in DPBST for 15 min at room temperature. Three washes with 1 mL blocking buffer (10% FBS, Sigma, F7524 in DPBST) were performed and the sample was blocked for 1 h at room temperature. Next, the sample was incubated with 200 μL primary antibody diluted

in blocking buffer overnight at 4°C. Three washes with 1 mL blocking buffer were performed for 5 min each and an additional blocking step with 200 μL 5% goat serum (Sigma, G9023) in blocking buffer was performed for 15 min at room temperature. The sample was incubated with 200 μL Atto647N secondary antibody diluted in 5% goat serum blocking buffer for 1 h at room temperature in the dark. Two washes with 1 mL blocking buffer and two washes with 1 mL DPBST were performed for 7 min each before the sample was placed in DPBST and imaged. Details of the antibodies used are listed in Table S1.

### Confocal fluorescence microscopy

Confocal imaging was performed on a Leica TCS SP8 microscope (Leica Microsystems GmbH) with 63x oil (NA: 1.4) or 63x water (NA: 1.2) immersion objective, for imaging clathrin topology and clathrin dynamics, respectively. Sample excitation was done using a supercontinuum laser (WLL, NKT Photonics) or a diode laser at 488 nm for mEos3.2, at 514 nm for EYFP or at 638 nm for Atto647N. Emission was captured on highly sensitive hybrid detectors (HyD SMD, Leica Microsystems GmbH) between 493 and 744 nm for mEos3.2-labeled samples, between 519 and 769 nm for EYFP-labeled samples, or between 519-638 nm and 643–779 nm for dual-color EYFP and Atto647N samples, respectively. Transmission images were captured simultaneously on a transmitted light detector. Image acquisition was performed with adaptive focus control activated, 512x512 or 1024x1024 pixels, 200 Hz line scan speed and 4-line averaging.

### Confocal clathrin topology

EYFP-CLTA cells transfected in a 35 mm disk with 14 mm glass-bottom insert, and when desired immunolabeled with CLTC-Atto647N, were imaged with previously described acquisition settings. For imaging, cells with predominantly lower fluorescence were visually selected to mitigate the impact of varying plasmid expression levels and extremely bright cells were specifically avoided. Images were processed using ImageJ 1.53c.[48,49] For clathrin topology quantification, clathrin clusters were identified in the EYFP-CLTA channel using a Trainable Weka Segmentation[51] that was applied on the whole dataset and their area was determined using the "Measure" function in the ROI Manager. Statistical analyses were performed using the open-source PlotsOfDifferences web app.[52,53] Colocalization of EYFP-CLTA and CLTC-Atto647N was determined by calculating the Pearson Correlation Coefficient of a transfected cell using the Huygens Professional Colocalization Analyzer Wizard (version 19.10 – Scientific Volume Imaging B.V.).

### Confocal clathrin dynamics

EYFP-CLTA cells transfected in a 6-well glass-bottom plate were gently washed 1x with 1 mL prewarmed DPBS (Thermo, 14200067), placed in prewarmed $CO_2$-independent medium consisting of DMEM-HEPES (Gibco, 21063029) supplemented with 10% FBS (Sigma, F7524) and 0.1% Gentamycin (Carl Roth, 2475.1) and imaged under incubation at 37°C and 5% $CO_2$. Continuous time-lapse imaging was performed for 20 min with an image acquisition every minute. For imaging, cells with predominantly lower fluorescence were visually selected to mitigate the impact of varying plasmid expression levels and extremely bright cells were specifically avoided. Images were taken according to previously described acquisition settings in three z-planes starting at the ventral membrane with 2 consecutive slices each 0.3 μm higher. In this article, only the z-slice corresponding to the ventral membrane is shown, which is the lowest z-position where fluorescent signal reaches a maximum brightness for the clathrin structures of interest. Discontinuous time-lapse imaging was performed over a time span of 8 h according to previously described acquisition settings with one image acquisition at each timepoint. The position of the cell was stored in the LAS X Navigator which was used to retrieve the same cell at consecutive timepoints. The temporal color-code denotes the specific timepoints at which the cells were imaged during the discontinuous time lapse. Between timepoints, the sample was transferred back to the humidified incubator at 37°C and 5% $CO_2$.

Temporal color-coded images were created using ImageJ 1.53g.[48,49] First, drift was corrected based on the fluorescent channel using the 3D drift correction plugin with standard settings and detection of slow drifts, sub pixel drift correction and edge enhanced images enabled. Afterward, fluorescence signal was corrected through time by resetting LUT to the max LUT value in each time frame. Finally, a temporal color code was applied for the fluorescent channel using the Temporal-Color code command that was adapted as suggested on the ImageJ forum (temporal color code bug 41323).

For quantification of 20-min clathrin dynamics at the ventral membrane, drift was corrected as described above and clathrin clusters were identified at every timepoint using a Trainable Weka Segmentation[51] that was applied on the whole dataset. Using a custom-written MATLAB script, clusters consisting of

more than ten pixels were classified at every timepoint either as "persistent" if minimally one of the pixels was present for the whole duration of the timelapse, or as "fluctuating" if this was not the case. For every timepoint, the percentage of persistent clusters, median area of persistent clusters, and median area of fluctuating clusters were calculated. Keeping in mind that the values for persistent clusters are derived from the same clusters at the different timepoints, but that the values for fluctuating clusters are more likely derived from different clusters at the different timepoints, median values across all timepoints were calculated. This resulted in one value for the percentage of persistent clusters, one value for the median area of persistent clusters, and one value for the median area of fluctuating clusters per measured cell. These median values were considered as datapoints in our analysis, and their statistical significance was determined the open-source PlotsOfDifferences web app.[52,53]

### PALM-TIRF fluorescence microscopy

mEos3.2-CLTA samples transfected in a 35 mm disk were gently washed 1x with 1 mL prewarmed DPBS and placed in 1 mL prewarmed HBSS (Gibco, 14025100). For imaging, cells with predominantly lower fluorescence were visually selected to mitigate the impact of varying plasmid expression levels and extremely bright cells were specifically avoided. For retrieval of the same cell in confocal and PALM-TIRF microscopy, mEos3.2-CLTA samples in a 35 mm disk with imprinted grid were first imaged in confocal microscopy as previously described, the same cell was retrieved using the grid coordinates and imaged on the PALM-TIRF microscope immediately afterward. PALM-TIRF imaging was performed on a home-build fluorescence widefield microscope with built-in through-the-objective TIRF illumination. This IX83 inverted microscope (Olympus IX83 frame S1F-3, Olympus Optical, Tokyo, Japan) has been previously described by Rocha et al.[54] and includes dichroic mirrors to combine the laser lines, neutral density filters to adjust the laser intensity (Newport Corporation, Irvine, CA, USA), a 10x beam expander (Linos, Qioptiq, Luxembourg), a focusing lens to enable TIRF illumination (f¼ 500 mm, BK 7, Newport Corporation), a 60× TIRF oil objective (Olympus Optical, NA: 1.45), a z488/561 dichroic mirror to separate excitation and emission, and a 2.5x projection lens (Olympus) placed before a 512x512 pixels EM-CCD camera (ImagEM, Hamamatsu Photonics, Hamamatsu, Japan) with a physical pixel size of approximately 107 nm.

For image acquisition, first a diffraction-limited image was taken by 488 nm excitation (200 mW 488 nm diode laser, Sapphire, Coherent) that passed a series of neutral density filters (1.62 OD) before reaching the sample, while emission was captured between 500 and 550 nm (HQ525/50 band-pass filter, Chroma Technology). For PALM imaging, mEos3.2 was stochastically activated using a 405 nm diode switching laser (100 mW laser Cube Coherent Inc., Santa Clara, CA, USA used at 3–6% intensity with neutral density filters 2.12 OD, resulting in an effective laser power of 0.46–2.70 μW at the objective). Stochastically activated fluorophores were excited with a 561 nm laser (200 mW laser, Sapphire, Coherent Inc. with neutral density filters 0.08 OD) and emission was captured between 575 and 615 nm (HQ595/40 band-pass filter, Chroma Technology). Image acquisition was performed by recording 2 x 5000 frames with an exposure time of 0.030530 s/frame. Transmission images were taken before, in between and after the 2 x 5000 frames to ensure the sample did not suffer from laser illumination during the imaging procedure. This imaging procedure takes approximately 10 min per imaged field of view and should be considered as a summed total of all blinking events across this time period. The image partly reflects clathrin dynamics, potentially leading to an overestimation of the number of dynamic structures (number of classical CCS), and to an overestimation of the number of localizations in persistent or reoccurring structures (NrPts of FCLs or clathrin hotspots) due to exchange with cytosolic clathrin.

For image reconstruction, a custom-written MATLAB algorithm (MATLAB R2022a) based on the open-source Localizer software package[55] was employed to localize the center positions of the emitters in each of the 10 000 frames by fitting them with a 2D Gaussian function with PSF standard deviation factor 1.8 and intensity selection sigma factor 25. By merging these retrieved positions, a super-resolved image with a lateral resolution of approximately 30–40 nm was obtained.

### PALM-TIRF cluster quantification

Clathrin topology was quantified in a PALM-TIRF dataset using a two-step MATLAB analysis that involved identification and classification of individual clathrin clusters. For identification of individual clathrin clusters, the DBSCAN data clustering algorithm was employed. First, images were gated to exclude background localizations falling outside the boundaries of the cell, which was defined by grouping nearby localizations into a region and selecting the largest region in the field of view. Then, the MATLAB DBSCAN

function[36] was executed for a minimum of 17 neighbors (MinPts) within a search radius (ε) of 0.55. These parameters were optimized based on visual observations on 6 different cellular regions from both poorly and highly metastatic cells by testing all possible combinations for MinPts = 8–23 and ε = 0.35–0.65 (Figure S9A for example). Note that suboptimal DBSCAN parameters give rise to an altered quantification result (Table S2), but that relative differences between non-metastatic and metastatic cells remain present. Since this approach identified also many extremely small clusters lying predominantly in noisy regions that correspond to single clathrin molecules rather than a CCS, only clusters with ≥50 localizations were retained for further analysis (Figure S9B).

To distinguish classical from alternative CCSs, identified clusters with ≥50 localizations were classified using a custom-written MATLAB algorithm. This identification was based on characteristics of individual clusters, more specifically the cluster area, the number of localizations within the cluster (NrPts, associated with cluster brightness), the cluster eccentricity (associated with cluster roundness), the cluster perimeter and the distance to the nearest neighboring cluster (MinDistance). Cluster eccentricity was calculated using the open-source MinVolEllipse function.[56] The classification model stated that if:

$$\frac{Area * \left(\frac{NrPts}{1000}\right) * Eccentricity * Perimeter}{MinDistance} > P90\ (classical\ CCSs)$$

the cluster was considered as an FCL, otherwise the cluster was classified as a classical CCS. The location of each of these terms in the numerator or denominator was carefully considered. Namely, a non-classical FCL is, from the literature or from our own observations (Figure S9C), expected to have a larger surface area, be brighter (larger NrPts), have a more elongated shape (eccentricity closer to unity), have a more irregular shape (larger perimeter) and would lie closer to other clusters (smaller MinDistance). Therefore, the model would yield a higher numerical output for an alternative FCL than for a classical CCS. This output was compared to a global threshold value (P90 classical CCSs) that was deduced from 1247 classical CCSs and 1042 FCLs that we manually selected from 3 to 5 different cellular regions containing predominantly classical CCSs and FCLs, respectively. The global threshold was set so that maximally 10% of the classical CCSs were incorrectly classified. This threshold was employed for quantification of both the KM12 and the SW model. The model was validated by visual confirmation to correctly identify the different structures. Cells that were too dim or too bright to allow for proper cluster identification and classification were excluded from the dataset.

This model resulted in a list of identified CCSs for every cell, in which each cluster was classified either as a classical CCS or as an alternative FCL. Cluster classification of the PALM-TIRF dataset for KM12 and SW cell models identified on average 429 CCSs per cell, adding to a total average of 15 003 CCSs per cell line (exact numbers can be found in Figure S10). The individual cluster properties that were employed for the cluster classification model were listed for every cluster, and their post-processing is described below. Firstly, for analysis of individual cluster area (Figure S9E), the median area of all classical CCSs and the median area of all alternative FCLs were calculated per cell. Considering the variance between different measured cells, these medians were considered as datapoints in our analysis. Medians were pooled per cell line while keeping classical CCS and FCL categories separated, and they were plotted and analyzed according to these categories. Secondly, to check whether cluster area depends on cell area (Figure S9F), individual cluster area was plotted in function of cell area for all the pooled cells while only distinguishing between classical CCS and alternative FCL categories. Thirdly, the ratio of (number FCLs per number classical CCSs) (Figure 4B) was calculated for each of the cells. Each ratio was considered as a datapoint in our analysis, they were pooled per cell line, plotted and analyzed according to these categories.

## QUANTIFICATION AND STATISTICAL ANALYSIS

Statistical analyses were performed using the open-source PlotsOfDifferences web app that determines statistical significances based on randomization of the data and therefore does not assume a specific distribution of the data.[52,53] Statistical details of experiments can be found in the figure legend where the number of datapoints (n), medians (x) and statistical significances (* significant difference for $p \leq 0.05$; ** significant difference for $p \leq 0.01$; *** significant difference for $p \leq 0.001$; ns non-significant difference for $p > 0.05$) are shown.